HHS Public Access

Author manuscript

ACS Appl Mater Interfaces. Author manuscript; available in PMC 2017 November 01.

Published in final edited form as:

ACS Appl Mater Interfaces. 2017 June 28; 9(25): 21133–21146. doi:10.1021/acsami.7b04351.

Redox-Responsive Polysulfide-Based Biodegradable Organosilica Nanoparticles for Delivery of Bioactive Agents

Seyyed Pouya Hadipour Moghaddam[†,§], **Jiban Saikia**[§], **Mostafa Yazdimamaghani**[†,§], and **Hamidreza Ghandehari**[*,†,‡,§]

[†]Department of Pharmaceutics and Pharmaceutical Chemistry, University of Utah, Salt Lake City, Utah 84112, United States

[‡]Department of Bioengineering, University of Utah, Salt Lake City, Utah 84112, United States

[§]Utah Center for Nanomedicine, Nano Institute of Utah, University of Utah, Salt Lake City, Utah 84112, United States

Abstract

Design and development of silica nanoparticles (SiO_2 NPs) with a controlled degradation profile promises effective drug delivery with a predetermined carrier elimination profile. In this research, we fabricated a series of redox-responsive polysulfide-based biodegradable SiO_2 NPs with low polydispersity and with variations in size (average diameters of 58 ± 7, 108 ± 11, 110 ± 9, 124 ± 9, and 332 ± 6 nm), porosity, and composition (disulfide vs tetrasulfide bonds). The degradation kinetics of the nanoparticles was analyzed in the presence of 8 mM glutathione (GSH), mimicking the intracellular reducing condition. Results indicate that porosity and core composition play the predominant roles in the degradation rate of these nanoparticles. The 108 nm mesoporous disulfide-based nanoparticles showed the highest degradation rate among all the synthesized nanoparticles. Transmission electron microscopy (TEM) reveals that nonporous nanoparticles undergo surface erosion, while porous nanoparticles undergo both surface and bulk erosion under reducing environment. The cytotoxicity of these nanoparticles in RAW 264.7 macrophages was evaluated. Results show that all these nanoparticles with the IC_{50} values ranging from 233 ± 42 to 705 ± 17 μg mL^{-1} do not have cytotoxic effect in macrophages at concentrations less than 125 μg mL^{-1}. The degradation products of these nanoparticles collected within 15 days did not show cytotoxicity in the same macrophage cell line after 24 h of incubation. *In vitro* doxorubicin (DOX) release was examined in 108 nm mesoporous disulfide-based nanoparticles in the absence and presence of 8 mM GSH. It was shown that drug release depends on intracellular reducing

[*]**Corresponding Author**: hamid.ghandehari@utah.edu. Postal Address: 5205 SMBB, 36 South Wasatch Drive, Salt Lake City, UT 84112, United States.

Supporting Information

The Supporting Information is available free of charge on the ACS Publications website at DOI: 10.1021/acsami.7b04351. STEM images and spectra, XRD graphs, TGA analyses, XPS survey spectra, FTIR spectra, additional degradation images, normalized degradation percentages, ESI-MS spectra, flow cytometry analyses, and atomic and mass percentages of the synthesized nanoparticles measured by XPS (PDF)

ORCID

Hamidreza Ghandehari: 0000-0002-9333-9964

Notes

The authors declare no competing financial interest.

conditions. Due to their ease of synthesis and scale up, robust structure, and the ability to control size, composition, release, and elimination, biodegradable SiO_2 NPs provide an alternative platform for delivery of bioactive and imaging agents.

Graphical abstract

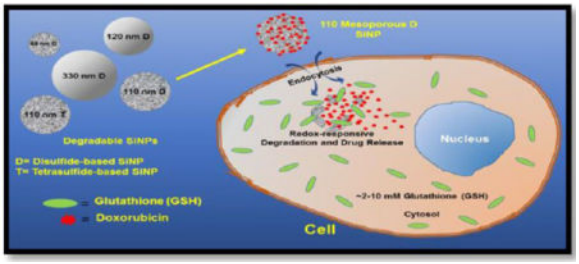

Keywords

silica nanoparticles; redox-responsive; biodegradable; glutathione; drug delivery

INTRODUCTION

Silica nanoparticles (SiO_2 NPs) have been investigated for therapeutic and imaging applications due to their mechanical and chemical stability and ease of synthesis and scale up, thereby providing the opportunity to fabricate composite materials.[1–3] Extensive research has been performed for loading drugs and imaging agents in mesoporous SiO_2 NPs or by attaching targeting ligands on the surface of these nanoparticles to facilitate localization in target tissues.[4–6] Controlled release of drugs from these systems has been accomplished by passive release, by attaching pH-sensitive or light-activated ligands, and by physical capping of the nanovalves.[7,8] It has been shown that factors such as size, porosity, surface charge, and surface functional groups can influence the biocompatibility of SiO_2 NPs.[9–11] Little is known however about the influence of the long-term deposition of SiO_2 NPs in tissues, cellular compartments, and subcellular organelles. It would be desirable to design and develop biodegradable silica nanocarriers for controlled drug delivery, where the degradation rate of the nanoparticles is controlled and the degradation products are eliminated from the body. Studies have shown that degradable silica nanoparticles can be made by incorporating enzymatically breakable amide-based linkers sensitive to the presence of proteases.[12,13] In another study, it was shown that biodegradable SiO_2 NPs with unprecedented drug payloads could be fabricated by using enzyme-sensitive oxamide/phenylene-based organosilica precursors.[14] Furthermore, researchers have indicated the use of breakable disulfide-based silsesquioxane nanoparticles for *in vitro* two-photon imaging and drug delivery to cancer cells.[15–17] Vivero-Escoto et al. have made degradable polysilsesquioxane nanoparticles using bis(trialkoxysilyl) derivatives of Gd(III) diethylenetriamine pentaacetate (Gd-DTPA) as efficient contrast agents for magnetic resonance imaging (MRI).[18] Additionally, Omar et al. have shown that degradable silica nanovectors can be synthesized using ultralarge pores spanning from 20 to 60 nm in diameter with high protein loading capacity.[19] These nanovectors can be degraded after 3

days of incubation in fetal bovine serum (FBS). However, studies to date for the preparation of biodegradable SiO_2 NPs do not address the degradation amount and kinetics of these nanoparticles and how the degradation products can affect the biological environment. Understanding the degradation rate of biodegradable SiO_2 NPs, its influence on drug release, and the fate of degradation products as a function of size, porosity, and composition is key for development of these systems for controlled drug delivery. In this study, a series of biodegradable nonporous and mesoporous, disulfide/tetrasulfide-based SiO_2 NPs were synthesized under controlled reaction conditions. The influence of size, porosity, and composition on *in vitro* degradation rate of the nanoparticles in the presence of glutathione (GSH) was evaluated. Release of doxorubicin (DOX) as a model drug, and cellular uptake, co-localization, and toxicity in RAW 264.7 macrophages were investigated.

RESULTS AND DISCUSSION

Synthesis and Characterization of SiO_2 NPs

In order to evaluate the effect of size, porosity, and composition on degradation kinetics, 5 spherical nanoparticles were synthesized using hydrolysis and co-condensation of the silane precursors in water/ethanol mixture under basic conditions. These nanoparticles were approximately 60 nm mesoporous disulfide-based SiO_2 NPs (designated as 60 Mesoporous D), 110 nm mesoporous disulfide-based SiO_2 NPs (designated as 110 Mesoporous D), 110 nm mesoporous tetrasulfide-based SiO_2 NPs (designated as 110 Mesoporous T), 120 nm nonporous disulfide-based SiO_2 NPs (designated as 120 Nonporous D), and 330 nm nonporous disulfide-based SiO_2 NPs (designated as 330 Nonporous D). Precursors used in the fabrication step were: tetraethyl orthosilicate (TEOS), bis[3-(triethoxysilyl)- propyl] disulfide (BTESPD), and bis[3-(triethoxysilyl)propyl] tetrasulfide (BTESPT) (Scheme 1).

Fabricated nanoparticles were then characterized using transmission and scanning electron microscopy (TEM and SEM, respectively) for evaluation of size, size distribution, and morphology. TEM and SEM images of nonporous and porous nanoparticles indicate their spherical morphology (Figure 1). On the basis of electron microscopy images, mesoporous nanoparticles had average diameters of 58 ± 7, 108 ± 11, and 110 ± 9 nm (Figure $1A_{1,2}$, $B_{1,2}$,$C_{1,2}$, respectively) and nonporous nanoparticles had average diameters of 124 ± 9 and 332 ± 6 nm (Figure $1D_{1,2}$,$E_{1,2}$, respectively). As evident in both microscopy images, highly uniform nanoparticles were synthesized. For mesoporous nanoparticles, pores can be observed in the corresponding TEM micrographs (Figure $1A_2$,B_2,C_2). As the nonporous nanoparticles grow in size, they become more spherical in morphology with a smoother surface (Figure $1E_2$: TEM panel). Reaction parameters that affected the physicochemical properties of the nanoparticles were concentration of precursors, how fast the precursors were added (time of injection), the amount of basic catalyst, CTAB concentration, temperature, stirring rate, and water to ethanol ratio.

Scanning transmission electron microscopy (STEM) was used to evaluate approximate atomic density within the nanoparticles using energy dispersive X-ray spectrometer (EDS) detector since it can zoom into one nanoparticle and scan over the sufficiently diluted sample in a rasterized pattern with high resolution. STEM images (Figure 2A) show homogeneous distribution of sulfur in the nanoparticles. All the other nanoparticles had the same

homogeneity in the distribution of sulfur, as shown in Figure S1. The overlaying images of O and S elucidate that nonporous nanoparticles have higher sulfur density than mesoporous particles since in the fabrication of these nanoparticles we just used BTESPD precursor without adding TEOS. STEM spectra also confirmed this higher sulfur density in nonporous nanoparticles in comparison to that in mesoporous particles (Figures 2B,C and S2).

Hydrodynamic diameters of the nanoparticles were measured using dynamic light scattering (DLS) (Table 1). The average hydrodynamic diameters of the nanoparticles in deionized (DI) water were: 79 ± 2, 165 ± 2, 162 ± 8, 148 ± 4, and 367 ± 2 nm, respectively. By dispersing the nanoparticles in RPMI media + 10% fetal bovine serum (FBS), hydrodynamic diameters of all the nanoparticles increased. This may be attributed to the formation of loose agglomerates which were reversible due to the presence of serum proteins covering the surface of these nanoparticles.[20] Therefore, the size of the nanoparticles may increase accordingly. These nanoparticles can then be easily redispersed by sonication. Zeta potential measurements were conducted at 25 °C and pH 7.2 (mimicking intracellular pH) in DI water. After dispersing the nanoparticles in DI water, negative zeta potential values of around −30 mV (Table 1) confirmed the presence of silanol (Si–OH) groups on the surface of these nanoparticles which become deprotonated ($Si–O^-$) in aqueous milieu. Comparing these numbers to zeta potential values of the nanoparticles obtained in media + 10% FBS, it can be deduced that high ionic strength (10 800 μS)[21] of RPMI media can reduce Debye length of the nanoparticles and hence decreases zeta potential of all the nanoparticles. The nanoparticles tended to precipitate within 30 min in phosphate-buffered saline (PBS). This may be ascribed to the hydrophobic organosilane groups (…–Si–**C–C–C**–S–S–**C–C–C**–Si–…) embedded in the framework of these nanoparticles. After dispersing them via sonication, the zeta potential of the nanoparticles decreased to lower values (Table 1). However, with approximately similar zeta potential values in media + 10% FBS, we did not observe any precipitation of the nanoparticles possibly due to the existence of proteins in FBS which form protein corona on the surface of the nanoparticles and reduce nanoparticle–nanoparticle interactions via steric repulsions.[22]

Nitrogen adsorption–desorption isotherm analyses for both nonporous and porous nanoparticles were conducted to investigate the Brunauer–Emmett–Teller (BET) specific surface area and Barrett–Joyner–Halenda (BJH) pore size distribution (Figure 3A–E). According to IUPAC classification of adsorption isotherms, both 60 and 110 nm disulfide-based nanoparticles exhibited type IV adsorption isotherms attributed to “mesoporous” nanoparticles with average pore diameters of 1.7 and 2 nm, respectively.[23] As shown in the corresponding isotherm plots, there is a hysteresis loop (demonstrating a narrow distribution of pores) which is usually related to capillary condensation in the mesopores and metastability of the gaseous phase at a high relative pressure (P/P_0).[24] The 110 nm tetrasulfide-based nanoparticles exhibited the same isotherm plot without having hysteresis at high relative pressure with an average pore diameter of 2.7 nm. This pore size difference may be due to the presence of longer chains including tetrasulfide (⋯–S–S–S–S–⋯) bonds during the formation of tetrasulfide-based nanoparticles which may alter pore diameter. Both 120 and 330 nm disulfide-based nanoparticles exhibited type III isotherm plots related to

nonporous nanoparticles. Type IV isotherms usually result from stronger fluid–solid interactions, while type III isotherms are correlated to weaker fluid–solid interactions.[25]

As expected, there was a noticeable difference between surface areas of mesoporous and nonporous nanoparticles. Table 2 includes data for the nanoparticles' surface area, total pore area, and average pore diameter of both mesoporous and nonporous nanoparticles. 120 Nonporous D and 330 Nonporous D nanoparticles had surface areas of 24 and 21 $m^2\ g^{-1}$, respectively, while for 60 Mesoporous D, 110 Mesoporous D, and 110 Mesoporous T nanoparticles, the surface areas were 614, 366, and 808 $m^2\ g^{-1}$, respectively. Results (Table 2) show that for 110 Mesoporous T nanoparticles, total pore area (313 $m^2\ g^{-1}$) was higher than for the other two mesoporous nanoparticles. This is probably due to the larger pore diameter of tetrasulfide-based nanoparticles in comparison with disulfide-based nanoparticles.

X-ray diffraction (XRD) graphs (Figures 3F and S3A,B) show that the mesoporous nanoparticles had disordered pore structure since they did not exhibit any characteristic peaks at low 2θ region, and all these mesoporous nanoparticles followed almost the same pattern in diffracting the incident X-rays. In this pattern, typical Bragg peaks which appear in regular nondegradable mesoporous SiO_2 NPs (such as MCM-41)[26,27] due to the formation of ordered hexagonal pores (Figure S3E) were not observed. This phenomenon is observed when hybrid nanoparticles are made by two different bissilylated precursors leading to the formation of so-called periodic mesoporous organosilicas (PMOs).[28,29] Another reason might be the presence of longer silyl chains in both BTESPD and BTESPT precursors which makes the formation of hexagonally ordered pores difficult.

Thermogravimetric analyses (TGA) (Figure S4) show more weight loss for biodegradable nanoparticles in comparison to that for nondegradable 100 nm Stöber SiO_2 NPs (designated as 100 Stöber). This phenomenon is related to the presence of organosilane matter (…–Si–**C–C–C**–S–S–**C–C–C**–Si–…) in the structure of degradable nanoparticles and could be attributed to the calcination of these organosilane groups. In nonporous nanoparticles, weight loss (ca. 53% for 120 nm and 47% for 330 nm) is higher than that for mesoporous nanoparticles which again reflects the absence of TEOS precursor during the fabrication step. Weight loss at less than 100 °C resulted from the loss of moisture from the nanoparticles.

For obtaining information about the composition of the degradable nanoparticles, X-ray photoelectron spectroscopy (XPS) was performed. XPS is a quantitative spectroscopic method that provides the elemental composition of the nanoparticles with an approximate depth of analysis of 1–10 nm from the surface of the nanoparticles. A higher number of S atoms (as shown in atomic/mass percentages and XPS survey spectra) are incorporated in 120 nonporous D and 330 nonporous D nanoparticles (Table S1 and Figure S5).

Fourier transform infrared (FT-IR) was conducted to confirm that the washing steps completely removed CTAB from the nanoparticles. On the basis of the FT-IR spectra (Figure S6), CTAB peaks at 2848 and 2914 cm^{-1} disappeared after washing the nanoparticles with acidic ethanol. The peaks at 1080 cm^{-1} could be attributed to the asymmetric vibrations of

Si–O–Si. The absorption band around 2940 cm^{-1} is due to CH_2 stretching in alkyl groups. Additionally, weak S–S stretching frequencies can be observed at wavenumbers of about 500 cm^{-1}.

In Vitro Degradation

The degradation profile of the synthesized nanoparticles was studied *in vitro* to evaluate the influence of size, porosity, and composition on the rate of degradation. The experiment was conducted for 15 days (at 37 °C and pH 7.2) and used 8 mM (Figure 4) and 8 μM (Figures S7 and S8) GSH to mimic intracellular and extracellular concentration of this reductant, respectively. GSH is a tripeptide (L-γ-glutamyl-L-cysteinyl-glycine) with an active pendant thiol group. GSH has a high intracellular concentration (~2–10 mM), while the extracellular values are about 3 orders of magnitude lower (~1–20 μM).[30–32] Results (Figure 4) indicate that the degradation of the mesoporous nanoparticles started from the first day. These nanoparticles had a much faster degradation rate than did their nonporous counterparts, most likely due to their higher surface area. TEM images suggest that nonporous nanoparticles underwent a surface erosion process while mesoporous nanoparticles underwent surface and bulk erosion (Figure 4). This implies that due to the higher surface area of mesoporous nanoparticles GSH can penetrate deeper in the pores and break S–S bonds by reducing them via its free thiol group. On the basis of both TEM (Figure 4) and inductively coupled plasma mass spectrometry (ICP-MS; Figure 5A), we did not observe any differences between the degradation rates of 120 Nonporous D and 330 Nonporous D nanoparticles due to a small difference between their surface areas (24 and 21 $m^2\ g^{-1}$, respectively). As shown in Figure 4, these nanoparticles broke into smaller size nanoparticles instead of being completely degraded. In the size range studied, size does not seem to be an important factor for the degradation of nonporous nanoparticles. It was observed that 60 Mesoporous D nanoparticles tend to agglomerate which reduce their effective exposure to GSH in solution (Figure S9). For 110 Mesoporous T nanoparticles, it can be assumed that the molar ratio of GSH to S–S–S–S bonds (containing 3 disulfide bonds) is 1:3, but this ratio is higher (1:1) in 110 Mesoporous D nanoparticles leading to higher degradation rate of disulfide- based nanoparticles in comparison to tetrasulfide-based nanoparticles. However, to ensure the nanoparticles having comparable size (ca. 110 nm), different precursor ratios were used in the fabrication step. XPS analyses (Table S1) indicate that the amount of S atoms incorporated in 110 Mesoporous D and 110 Mesoporous T nanoparticles is 4.68 and 2.20%, respectively. Additionally, TGA graph (Figure S4) confirms that higher portion of organosilane part is incorporated in 110 Mesoporous D nanoparticles than that in 110 Mesoporous T nanoparticles. This could decrease degradation rate of tetrasulfide-based nanoparticles in comparison to the same size disulfide-based nanoparticles. As indicated in Figure 4, the controls containing nanoparticle suspension without GSH did not show any degradation within the 15 day study period.

It should be noted that our degradation study was done under static conditions, while *in vivo* settings are dynamic. In the body there is an equilibrium between oxidized (GSSG) and reduced (GSH) glutathione via glutathione peroxidase/reductase enzymes.[33] Hence, the degradation rate of these nanoparticles would be higher as the concentration of GSH is kept constant *in vivo*. In addition, intracellular environment contains a class of enzymes called

thioredoxins (Trx) which could facilitate the degradation of polysulfide-based nanoparticles.[34]

It must be noted that in some cases (for example, in 110 Mesoporous D nanoparticles) some nanoparticles degraded even within the first 48 h in 8 mM GSH (Figure S10). This suggests the number of S–S bonds existing in the nanoparticles and their spatial exposure to GSH are both important factors for degradation. Therefore, some nanoparticles might have more S–S bonds in their structure during the fabrication step and have higher degradation rate.

For quantitative evaluation of the degradation kinetics of the nanoparticles, ICP-MS was used (Figure 5A). In addition, we assessed degradation rate of the nanoparticles over time by measuring the amount of GSH consumption using *ortho*-phthalaldehyde (OPA) (Figure 5B). OPA can selectively bind to nitrogen and sulfur atoms of GSH with its aldehyde groups forming isoindole-GSH which is highly fluorescent at excitation/emission wavelengths of 340/420 nm (Figure 5C).[35] As a control, we suspended the regular Stöber SiNP in 8 mM GSH solution and observed that there was no GSH consumption within the 15 days since these nanoparticles do not possess any S–S bonds in their structure and they were made by only the TEOS precursor.

In both assays (Figure 5A,B), it was found that there were statistically significant differences between nonporous and mesoporous nanoparticles ($P_{value} < 0.05$) which clearly shows the influence of porosity on degradation. In addition, we measured the normalized nanoparticles degradation percentages over the 15 day period of study (Figure S11), and as shown, 110 Mesoporous D had the highest amount of degradation up to 14%. For better understanding of the degradation kinetics of the nanoparticles, they were evaluated in DI water without GSH under the same conditions and constant rotation over 15 days. It was observed that 60 Mesoporous D nanoparticles had the highest dissolution (6.31 μg mL^{-1}) and 330 Nonporous D nanoparticles had the lowest dissolution (1.17 μg mL^{-1}) after 15 days which can be attributed to the size and surface area of these nanoparticles (614 and 21 m^2 g^{-1}, respectively).

In Vitro Cytotoxicity

For evaluating cellular toxicity of the nanoparticles, we tested both the intact nanoparticles and their corresponding degradation products in RAW 264.7 macrophages in a wide range of concentration (8–1000 μg mL^{-1}). This wide range was selected to identify both safe and toxic concentrations of these nanoparticles. RAW 264.7 macrophages are mouse leukemic macrophage-like cell lines derived from BALB/c mice with high phagocytic activity. We chose the RAW 264.7 cell line since they maintain many of the features of macrophages such as high phagocytic activity and represent the physiological scavengers when foreign nanoparticles are exposed *in vivo*. Macrophages participate in inflammatory and immunological processes. Our previous studies had also demonstrated that macrophages take up silica nanoparticles to a higher extent than other cells such as epithelial cells.[36,37] Toxicity of SiO_2 NPs can occur by generation of reactive oxygen species via silanol groups which initiates intracellular oxidative stress, or hydrogen bonding and electrostatic interactions between SiO_2 NPs SiOH/SiO$^-$ and proteins or phospholipids existing in cell membranes.[38–40] Cell counting kit-8 (CCK-8) and lactate dehydrogenase (LDH) assays

were used for evaluating cytotoxicity. Results demonstrate that toxicity of these nanoparticles were all concentration-dependent (Figure 6A,B). On the basis of CCK-8 assay, 110 Mesoporous D nanoparticle did not exhibit any toxic effect at concentrations less than 250 μg mL^{-1} after 24 h of exposure (ca. 100% cell viability). The toxicity of this nanoparticle started at concentrations above 250 μg mL^{-1} in which 1000 μg mL^{-1} decreased cell viability to ca. 30%. 110 Mesoporous T nanoparticles appeared to be nontoxic at concentrations less than 125 μg mL^{-1}, but above this concentration, moderate toxicity was observed. Cell viability decreased significantly at concentrations above 500 μg mL^{-1} (ca. 25% viability). In contrast, 60 Mesoporous D decreased relative viability of the cells to ca. 85% at concentrations of 100–125 μg mL^{-1}, while at concentrations less than 100 μg mL^{-1}, they did not affect the cells negatively. Approximately 50% of the cells died by treatment with 250 μg mL^{-1} of this nanoparticle followed by more viability reduction as a result of increasing the concentration to 1000 μg mL^{-1}. For 120 Nonporous D, relative viability of the cells was reduced to ca. 85% at concentrations of 85–125 μg mL^{-1}. The latter nanoparticle did not show toxic effects at concentrations less than 85 μg mL^{-1}, though this nanoparticle was highly toxic at concentrations greater than 250 μg mL^{-1}. LDH cytotoxicity assay confirmed that membrane rupture and subsequent LDH release was increased to 25% at concentrations greater than 125 μg mL^{-1} (specifically for 110 Mesoporous T, 120 Nonporous D, and 330 Nonporous D nanoparticles). These observations confirm the potential utility of these nanoparticles as delivery vehicles for carrying anticancer drugs (e.g., for delivery, 10 mg kg^{-1} of DOX in mouse) or imaging agents *in vivo* (e.g., iron nanocomposites). Further studies are required to evaluate subacute toxicity, chronic toxicity, and genotoxicity of these nanoparticles both *in vitro* and *in vivo*.

After determining cytotoxicity of these intact nanoparticles, toxicity of degradation products in supernatant solution was evaluated in RAW 264.7 macrophages using CCK-8 (Figure 6C). Electrospray ionization mass spectroscopy (ESI-MS) was used to see if we could identify what degradation fragments were present in supernatants (Figure S12). ESI-MS analyses of the precursors (Figure S12A–C) exhibited specific peaks which were related to the molecular weights of pure TEOS, BTESPD, and BTESPT but in the analyses of the degradation products, many peaks having different heights (percentages) appeared in the corresponding spectra (Figure S12D–H). This shows the presence of various degradation fragments in the supernatant solution. Supernatant solutions were directly added to RAW 264.7 macrophages after being collected at each time point (0, 1, 4, 7, and 15 days). Interestingly, as demonstrated in Figure 6C, more than 85% cell viability was observed after 24 h of incubation at all the time points. Cell death of 10–15% may be the result of alkyl containing silicate (SiO_4^{2-}) groups released from the nanoparticles.

Using the CCK-8 assay, IC_{50} values (Table 3) spanned approximately from 233 ± 42 to 705 ± 17 μg mL^{-1} for 110 Mesoporous T and 110 Mesoporous D nanoparticles, respectively. Both IC_{50} and fast degradation rate of 110 Mesoporous D nanoparticles suggest that this nanocarrier could be a good choice for further *in vivo* evaluation and its potential use for delivery of anticancer drugs to tumor tissues via enhanced permeability and retention (EPR) effect.[41]

In Vitro Cell Uptake, Co-Localization, and Release

Cell uptake and intracellular co-localization of the nanoparticles were evaluated using TEM and confocal laser scanning microscopy (CLSM), respectively (Figures 7 and 8A). For cell uptake, 80 μg mL^{-1} nanoparticles was added to RAW 264.7 macrophages incubated for 4 and 24 h. This concentration was selected since all the nanoparticles showed no toxicity in RAW 264.7 macrophages at this concentration after incubation for 24 h. Results (Figure 7) show that the nanoparticles (especially 110 Mesoporous D and 330 Nonporous D) were taken up by the macrophage cells in a time-dependent pattern. This higher uptake of 110 Mesoporous D and 330 Nonporous D nanoparticles was consistent with flow cytometry results for FITC-doped nanoparticles in which both larger nonporous and mesoporous nanoparticles were taken up more than the smaller nanoparticles (Figures S13 and S14).[42] As depicted in Figure 7, more nanoparticles were endocytosed by macrophages after 24 h of incubation. The internalized nanoparticles seem to be engulfed in endosomal or endolysosomal vacuoles. Additionally, a few nanoparticles appear to be isolated without vacuole encapsulation within the cytoplasm (Figure 7, green arrows). Cells without nanoparticle treatment were used as controls.

The intracellular fate of the nanoparticles after endocytosis was investigated using FITC-doped nanoparticles. As presented in Figure 8A, most of the nanoparticles accumulated in the endolysosomal compartments and in the perinuclear regions after incubation for 24 h in RAW 264.7 macrophages. Regarding endolysosomal pathway, reduction of the disulfide bonds can also occur in endocytic compartments.[43–45] The presence of gamma interferon-inducible lysosomal thiol-reductase (GILT) enzyme in the lysosomal compartments can facilitate the degradation of polysulfide-based nanoparticles.[46,47] This enzyme has optimal reductase activity at the acidic pH of lysosomes.[48]

Release of DOX as a model compound was evaluated from 110 Mesoporous D nanoparticles that showed the fastest degradation rate. Results show that there is a statistically significant difference between the amount of DOX released from the nanoparticles in the presence and absence of GSH (Figure 8B). As demonstrated, in the absence of GSH the drug is released from the pores, but in the presence of GSH, release occurs both from the pores as well as due to the degradation of the nanoparticles.

CONCLUSIONS

In this work, we have successfully synthesized and characterized highly uniform redox-responsive polysulfide-based biodegradable silica nanoparticles with differences in size, porosity, and composition. We demonstrated that the mesoporous nanoparticles undergoing surface and bulk erosion had a higher degradation rate than nonporous nanoparticles. These findings were confirmed by ICP-MS and GSH-OPA assays by measuring the amount of silicon release and GSH consumption, respectively. According to TEM and CLSM, the nanoparticles were taken up by macrophages in a time-dependent manner and trapped in endolysosomal compartments. Results show that 110 Mesoporous D nanoparticles had a higher degradation rate in response to GSH with lower cytotoxicity in RAW 264.7 macrophages. It was shown that the degradation products did not exhibit negative effects on cell viability within 15 days. When DOX was loaded in 110 Mesoporous D nanoparticles, a

greater amount of the drug was released in the presence of 8 mM GSH. Degradable silica nanoparticles show promise in controlled delivery of bioactive agents. The next logical steps are accurate characterization of the degradation products and optimizing degradation rate for specific delivery applications.

EXPERIMENTAL PROCEDURES

Materials

The following compounds were purchased from Sigma-Aldrich, Inc. (St. Louis, MO): aminopropyltriethoxysilane (APTES, ≥98.0%), cetyltrimethylammonium bromide (CTAB, ≥99.0%), tetraethyl orthosilicate (TEOS, ≥99.0% GC), Triton X-100, sodium hydroxide (NaOH), bisbenzimide Hoechst No. 33342, fetal bovine serum (FBS), and glutathione (GSH). TrypLE, fluorescein isothiocyanate (FITC), LDH Cytotoxicity Assay Kit, and LysoTracker Deep Red were purchased from Thermo Fisher Scientific (Grand Island, NY). Bis[3-(triethoxysilyl)propyl] disulfide (BTESPD, 90.0%) and bis[3-(triethoxysilyl)propyl] tetrasulfide (BTESPT, ≥90.0%) were received from Gelest, Inc. (Morrisville, PA). Doxorubicin hydrochloride salt (DOX, >99.0%) was acquired from LC Laboratories (Woburn, MA). *ortho*-Phthalaldehyde (OPA) and glutathione assay buffer were purchased from BioVision, Inc. (Milpitas, CA). RPMI media, hydrochloric acid (ACS-grade BDH, 36.5–38.0%), and PBS biotechnology-grade tablets were received from VWR (Radnor, PA). Absolute ethanol (200 proof) and ethanol 95% were purchased from Decon Laboratories, Inc. (King of Prussia, PA) and Fisher Science Education (Nazareth, PA), respectively. Trypan Blue Stain 0.4% was obtained from Invitrogen (Carlsbad, CA). Ammonium hydroxide (NH_4OH, 28–30% as NH_3) was received from EMD Millipore Corporation (Billerica, MA). RAW 264.7 macrophage cell line (ATCC TIB-71) was obtained from American Type Culture Collection (ATCC, Manassas, VA). CCK-8 cytotoxicity assay kit was received from Dojindo (Rockville, MD). All materials were used as received and without further purification.

Methods

Synthesis of Polysulfide-Based Nanoparticles—For preparing 60 nm mesoporous disulfide-based nanoparticles, 110 mL of DI water, 10 mL of ethanol (200 proof), 220 mg of CTAB, and 490 μL of sodium hydroxide (2 M) were mixed in 250 mL round-bottomed flask at 80 °C at a stirring rate of 500 rpm for 30 min. Then, the stirring rate was increased to 1600 rpm, and TEOS/BTESPD mixture with the molar ratio of 4.8:1 was added. The reaction was left under stirring for 6 h. For fabricating 110 nm mesoporous disulfide-based nanoparticles, 110 mL of DI water, 10 mL of ethanol (200 proof), 220 mg of CTAB, and 900 μL of sodium hydroxide (2 M) were mixed in 250 mL round-bottomed flask at 80 °C at a stirring rate of 500 rpm for 30 min. Then, the stirring rate was increased to 1400 rpm, and TEOS/BTESPD mixture with the molar ratio of 4.8:1 was added. The reaction was allowed to stir for 6 h.

For synthesizing 110 nm mesoporous tetrasulfide-based nanoparticles, 110 mL of DI water, 10 mL of ethanol (200 proof), 220 mg of CTAB, and 900 μL of sodium hydroxide (2 M) were mixed in 250 mL round-bottomed flask at 80 °C at a stirring rate of 500 rpm for 30

min. Then, the stirring rate was increased to 1400 rpm, and TEOS/BTESPT mixture with the molar ratio of 6.6:1 was added. The reaction was left under stirring for 6 h. After synthesis, all mesoporous nanoparticles were washed thoroughly with water and ethanol for several times. CTAB was removed by suspending the nanoparticles in acidic ethanol (1 mL of HCl 36.5% in 30 mL of ethanol 100%) and kept under reflux at 80 °C for 6 h. The nanoparticles were then washed thoroughly with water/ethanol 95% mixture, precipitated by centrifugation using Sorvall RC-5B Refrigerated Superspeed Centrifuge (Du Pont Instruments Ltd., Wilmington, DE) at 18 000 rpm for 15 min, and stored in ethanol for further use.

Nonporous nanoparticles were synthesized as follows: For 120 nm nanoparticles, 10 mL of DI water, 4 mL of ethanol (200 proof), 64 mg of CTAB, and 18 μL of sodium hydroxide (2 M) were mixed in 25 mL round-bottomed flask at 40 °C at a stirring rate of 500 rpm for 30 min. Then, the stirring rate was increased to 1600 rpm, and 240 μL of BTESPD (diluted in ethanol 1:3) was added dropwise. The reaction was allowed to stir for 4 h. For 330 nm, 10 mL of DI water, 4 mL of ethanol (200 proof), 32 mg of CTAB, and 25 μL of sodium hydroxide (2 M) were mixed in 25 mL round-bottomed flask at 40 °C at stirring rate of 500 rpm for 30 min. Afterward, the stirring rate was increased to 1400 rpm, and 240 μL of BTESPD (diluted in ethanol 1:1) was added dropwise. The reaction was left under stirring for 4 h. Nanoparticles were then washed extensively with water/ethanol 95% mixture, collected by centrifugation at 18 000 rpm for 15 min, and stored in ethanol for further use.

For the synthesis of nondegradable Stöber nanoparticles, 100 mL of ethanol (200 proof), 2.8 mL of DI water, and 3.6 mL of ammonium hydroxide were mixed at room temperature and stirred at 400 rpm for 10 min. Afterward, 3.5 mL of TEOS was added dropwise and the reaction was left under stirring for 24 h. The product was washed twice with water/ethanol 95% mixture, collected by centrifugation at 18 000 rpm for 15 min, and stored in ethanol for further use.

For the fabrication of nondegradable mesoporous nanoparticles, 200 mg of CTAB was dissolved in 70 mL of DI water, and 5 mL of ammonium hydroxide was added to the mixture. The mixture was stirred at room temperature for 1 h at 300 rpm. 4.8 mL of TEOS was then added dropwise under stirring at 300 rpm and left stirring for 4 h. The product was washed thrice with water/ethanol 95% mixture, suspended in acidic ethanol (1 mL of HCl 36.5% in 30 mL of ethanol 100%), and heated to 80 °C under reflux for 6 h to remove the surfactant.

Physicochemical Characterization of Nanoparticles—Morphology and size of the nanoparticles was explored by electron microscopy methods. Transmission electron microscopy (TEM) and scanning electron microscopy (SEM) images were taken by FEI Tecnai 12 transmission electron microscope (Hillsboro, OR) operating at 120 kV and FEI Quanta 600F scanning electron microscope (Hillsboro, OR) operating at 20 kV, respectively. X-ray diffraction (XRD) patterns of all nanoparticles were investigated on a Bruker D2 Phaser X-ray diffractometer (Bruker AXS, Madison, WI) using Cu Kα radiation (λ = 0.1542 nm) at 45 kV and 40 mA. The XRD spectra were recorded at a scanning speed of 0.01°/s, with a step size of 0.02° in a 2θ scattering angle and in a range of 0–8. Fourier

transform infrared (FT-IR) spectra were obtained on a Varian 3100 FT-IR Excalibur Series Spectrometer (Randolph, MA) with attenuated total reflectance mode to confirm complete removal of the surfactant (CTAB). Hydrodynamic diameter and zeta potential measurements were conducted by dynamic light scattering (DLS) in a Malvern Instruments Zetasizer Nano ZS (Malvern Instruments Ltd., Worcestershire, U.K.). Measurements were performed in triplicate. Nitrogen adsorption–desorption isotherm analyses were performed at −196 °C on a Micromeritics ASAP 2020 (Norcross, GA) for measuring surface area and pore size. All samples were dried at 100 °C overnight prior to analysis. Pore volume and pore size distributions were obtained from an adsorption branch by using the Barrett–Joyner–Halenda (BJH) method. The Brunauer–Emmett–Teller (BET) specific surface areas were measured via adsorption data at P/P_0 = 0.05–0.20. Scanning transmission electron microscopy (STEM) images and spectra of the nanoparticles were acquired on JEOL JEM-2800 (Akishima, Tokyo, Japan) scanning transmission electron microscope with dual energy dispersive X-ray spectrometer (EDS) detectors at an electron beam energy of 200 kV. Sample preparation was done by drop casting the nanoparticles on a carbon coated TEM grid. X-ray photoelectron spectroscopy (XPS) analyses of the nanoparticles were performed by Axis Ultra DLD instrument (Kratos Analytical, Manchester, UK). For analyses, the samples were mounted on a C tape and pumped overnight in the load lock before introduction into the analysis chamber. A mono Al source was employed. Survey scans were collected with a pass energy of 160 eV, step size of 1 eV, and dwell time of 200 ms. High-resolution region scans were collected with a pass energy of 40 eV, 0.1 eV step size, and 400 ms dwell time. Data were processed using CASA XPS software. Thermogravimetric analyses (TGA) were performed using a TA Instruments hi-resolution TGA 2950 Thermogravimetric Analyzer (New Castle, DE). All TGA experiments were performed under N_2 atmosphere from 35 to 800 °C at a heating rate of 20 °C/min.

Degradation Studies—Degradation of all the synthesized nanoparticles (80 μg mL^{-1}) was evaluated mimicking intracellular and extracellular GSH concentrations (8 mM and 8 μM, respectively) in DI water at 37 °C under constant rotation at 18 rpm using ProBlot 100 hybridization incubator. At predetermined times points (0, 1, 4, 7, and 15 days), samples were collected for TEM, ICP-MS, ESI-MS, and OPA analyses. For TEM, water suspensions containing nanoparticles were drop-cast onto Formvar coated Cu grids and allowed to dry prior to visualization using FEI Tecnai T12 operating at 120 kV.

For ICP-MS, an Agilent 7500ce ICP-MS instrument (Santa Clara, CA) was used. Aliquots of the reaction suspensions (1 mL each) were collected and stored in 1.5 mL centrifuge tubes followed by centrifugation (Centrifuge 5415 D Eppendorf, Hauppauge, NY) at 13 000 rpm for 15 min. Then, 600 μL of the supernatants were collected, transferred into new 1.5 mL vials, centrifuged at 13 000 rpm for 15 min, and 400 μL of supernatants were collected again to ensure that there were no nanoparticles left in the supernatants. Aliquots of the samples were then taken (200 μL) and diluted to 2 mL with ultrapure water. Finally, 20 uL of cesium internal standard was added as an instrumental control. Silicon assays were performed in triplicate.

For ESI-MS analyses, supernatants containing degradation products were diluted in methanol and analyzed by Waters ACQUITY TQ Detector (Waters Corporation, Milford,

MA) mass spectrometer. The instrument operated in electrospray positive ion mode. The ion source temperature was set at 150 °C and the desolvation temperature was 350 °C. The cone and the capillary voltages were 3 V and 3 kV, respectively.

For OPA study, 10 μL of the collected samples were mixed with 10 μL OPA solution and 180 μL buffer. The fluorescence was then measured at excitation/emission wavelength of 340/420 nm using SpectraMax M_2 (Molecular Devices, Sunnyvale, CA) microplate reader. Measurements were conducted in triplicate.

Cytotoxicity Assays—Cytotoxicity of the intact nanoparticles was tested on RAW 264.7 macrophages. Cells were cultured at 37 °C in 5% CO_2 in RPMI with 10% FBS. Then, the cells were stained using Trypan Blue Stain 0.4% and read by Invitrogen Countessautomated cell counter (Thermo Fisher Scientific Corporation, Grand Island, NY). For the cytotoxicity evaluation, cells were seeded onto 96-well plates with the density of 6000 cells/well and allowed to grow for 24 h. After 24 h, the media was replaced, and the cells were washed with PBS. Fresh media containing 10% FBS was then added with varying nanoparticle concentrations ranging from 8 to 1000 μg mL^{-1}. Wells with media and Triton X-100 (without nanoparticles) were utilized as negative and positive controls, respectively. The cells were then incubated for 24 h, the media aspirated, and the cells washed twice with PBS. Cell viability was measured using CCK-8 cytotoxicity assay kit according to an established protocol, and absorbance was measured at 450 nm with SpectraMax M_2 microplate reader. For membrane integrity test, LDH Cytotoxicity Assay Kit was used according to the manufacturer's protocol. Assays were performed in triplicate.

For investigating cell toxicity of degradation products, collected supernatants at different time points were added to 96-well plates (50 μL of supernatant + 100 μL of media containing 10% FBS). As previously mentioned, cells were incubated for 24 h at 37 °C in 5% CO_2 followed by aspirating the media and washing the cells twice with PBS. Cell viability was measured with CCK-8 cytotoxicity assay kit at 450 nm using SpectraMax M_2 microplate reader. Experiments were performed in triplicate.

Cell Uptake via TEM—Uptake of the nanoparticles by RAW 264.7 macrophages were investigated using TEM. Cells were grown on ACLAR sheets in 6-well plates (180 000 cells/well) and treated with 80 μg mL^{-1} of nanoparticles. Controls were treated by media containing 10% FBS. After incubation for 4 and 24 h at 37 °C in 5% CO_2, cells were washed 3 times with PBS. One mL of fixing solution (2.5% glutaraldehyde + 1.0% paraformaldehyde) was added to the cells, and the mixture was incubated at room temperature for 30 min followed by 4 °C overnight. Ultrathin sections of control and treated cells were imaged by FEI Tecnai T12 operating at 120 kV.

Co-Localization via Confocal Laser Scanning Microscopy (CLSM)—To evaluate the co-localization of the nanoparticles, CLSM was employed and images were obtained by Olympus FluoView FV1000 confocal microscope (Olympus Corporation, Shinjuku, Tokyo, Japan) at 60× magnification. FITC-doped nanoparticles were synthesized by the following procedure: First, 1.7 mg of FITC and 9 μL of APTES were mixed in 5 mL of ethanol (200 proof) and stirred for 30 min. Then, known amounts (the same as what we used for

fabricating intact nanoparticles) of BTESPD (for nonporous nanoparticles), TEOS/BTESPD (for mesoporous disulfide-based nanoparticles), and TEOS/BTESPT (for mesoporous tetrasulfide-based nanoparticles) were added to this solution. In another flask CTAB, sodium hydroxide, ethanol (200 proof), and water were mixed together with amounts similar to what was mentioned in the "Synthesis of Polysulfide-Based Nanoparticles" section. Finally, the solution containing silane sources was added to this flask, kept under vigorous stirring for 6 h, and the flasks were wrapped with aluminum foil to prevent FITC from bleaching.

Two-chambered cover glasses (Lab-Tek Chambered #1.0 Borosilicate Coverglass System) were used for this experiment. After seeding the chambers with cells (80 000 cells/chamber), they were allowed to grow for 24 h at 37 °C in 5% CO_2. Next, the media was removed, and FITC-doped nanoparticles (80 μg mL^{-1}) were added to each chamber and incubated for 24 h. Then, the cells were washed 3 times with PBS. LysoTracker Deep Red (50 nM) was then added to each chamber, and the cells were incubated for 1 h. After that, Hoechst 33342 (2 μg mL^{-1}) was added to the chambers, and the cells were incubated for another 10 min. Last, the staining solutions were removed, and the cells were washed 3 times with PBS. The excitation wavelength for FITC, Hoechst, and LysoTracker Deep Red were adjusted to 495, 350, and 647 nm, respectively.

Flow Cytometry—To quantitate the uptake of the nanoparticles by RAW 264.7 macrophages, flow cytometry using BD FACSCanto System (BD Biosciences, San Jose, CA) was used. 180 000 cells/well were seeded onto 6-well plates and incubated for 24 h at 37 °C in 5% CO_2. Then, the media was removed, and FITC-doped nanoparticles (80 μg mL^{-1}) were added to each chamber and incubated for 24 h. Control wells were treated with the same volume of media. Afterward, cells were washed 3 times with cold PBS followed by addition of 600 μL of TrypLE and incubation for 5 min. The cells were then centrifuged at 2500 rpm for 5 min and washed with cold PBS. Finally, the cells were resuspended in cold PBS + 2% FBS prior to analysis. Measurements were performed in triplicate.

Drug Loading and Release—110 Mesoporous D was selected as model degradable nanoparticle for release study. A known concentration of DOX was mixed with 110 Mesoporous D and allowed to stir for 24 h at room temperature. Afterward, the nanoparticles were removed by centrifugation at 13 000 rpm for 15 min and washed 3 times with DI water for removing the unbound trapped drug within the nanoparticles. Then, DOX-loaded nanoparticles were dispersed in DI water (pH 6.5) containing 8 mM GSH. Vials without GSH were used as control. Subsequently, the suspension was kept under constant stirring at 37 °C. Equal aliquots were taken out at specific time points, centrifuged at 13 000 rpm for 15 min, and the supernatants used to measure the amount of the released drug with excitation wavelength at 480 nm. The concentrations were all determined using DOX standard curve. Measurements were performed in triplicate.

Statistical Analysis—Data are expressed as mean ± standard deviations (SD) for at least three separate experiments. The difference between multiple groups was analyzed by ANOVA. For comparison between two groups, Student's *t* test was used. The difference compared to control was considered significant at $P_{value} < 0.05$.

Supplementary Material

Refer to Web version on PubMed Central for supplementary material.

Acknowledgments

We greatly acknowledge financial support from the National Institute of Environmental Health Sciences of the NIH (R01ES024681), the University of Utah Nanotechnology Training Program Fellowship (Seyyed Pouya Hadipour Moghaddam), and College of Pharmacy Skaggs Fellowship (Mostafa Yazdimamaghani). This work made use of the University of Utah shared facilities of the Micron Microscopy Suite and the University of Utah USTAR shared facilities supported in part by the MRSEC Program of the NSF under Award No. DMR-1121252.

References

1. Wu X, Wu M, Zhao JX. Recent Development of Silica Nanoparticles as Delivery Vectors for Cancer Imaging and Therapy. Nanomedicine. 2014; 10:297–312. [PubMed: 24028896]
2. Ma M, Yan F, Yao M, Wei Z, Zhou D, Yao H, Zheng H, Chen H, Shi J. Template-Free Synthesis of Hollow/Porous Organosilica–Fe3o4 Hybrid Nanocapsules toward Magnetic Resonance Imaging-Guided High-Intensity Focused Ultrasound Therapy. ACS Appl Mater Interfaces. 2016; 8:29986–29996. [PubMed: 27774787]
3. Lee JE, Lee N, Kim T, Kim J, Hyeon T. Multifunctional Mesoporous Silica Nanocomposite Nanoparticles for Theranostic Applications. Acc Chem Res. 2011; 44:893–902. [PubMed: 21848274]
4. Wu L, Wu M, Zeng Y, Zhang D, Zheng A, Liu X, Liu J. Multifunctional Peg Modified Dox Loaded Mesoporous Silica Nanoparticle@Cus Nanohybrids as Photo-Thermal Agent and Thermal-Triggered Drug Release Vehicle for Hepatocellular Carcinoma Treatment. Nanotechnology. 2015; 26:025102. [PubMed: 25517859]
5. Cao M, Wang P, Kou Y, Wang J, Liu J, Li Y, Li J, Wang L, Chen C. Gadolinium(Iii)-Chelated Silica Nanospheres Integrating Chemotherapy and Photothermal Therapy for Cancer Treatment and Magnetic Resonance Imaging. ACS Appl Mater Interfaces. 2015; 7:25014–23. [PubMed: 26418578]
6. Wu X, Han Z, Schur RM, Lu Z-R. Targeted Mesoporous Silica Nanoparticles Delivering Arsenic Trioxide with Environment Sensitive Drug Release for Effective Treatment of Triple Negative Breast Cancer. ACS Biomater Sci Eng. 2016; 2:501–507.
7. Tarn D, Ferris DP, Barnes JC, Ambrogio MW, Stoddart JF, Zink JI. A Reversible Light-Operated Nanovalve on Mesoporous Silica Nanoparticles. Nanoscale. 2014; 6:3335–3343. [PubMed: 24519642]
8. Tarn D, Xue M, Zink JI. pH-Responsive Dual Cargo Delivery from Mesoporous Silica Nanoparticles with a Metal-Latched Nanogate. Inorg Chem. 2013; 52:2044–2049. [PubMed: 23391170]
9. Fujiwara K, Suematsu H, Kiyomiya E, Aoki M, Sato M, Moritoki N. Size-Dependent Toxicity of Silica Nano-Particles to Chlorella Kessleri. J Environ Sci Health, Part A: Toxic/Hazard Subst Environ Eng. 2008; 43:1167–73.
10. Nabeshi H, Yoshikawa T, Arimori A, Yoshida T, Tochigi S, Hirai T, Akase T, Nagano K, Abe Y, Kamada H, Tsunoda S-i, Itoh N, Yoshioka Y, Tsutsumi Y. Effect of Surface Properties of Silica Nanoparticles on Their Cytotoxicity and Cellular Distribution in Murine Macrophages. Nanoscale Res Lett. 2011; 6:93. [PubMed: 21711578]
11. Yu T, Greish K, McGill LD, Ray A, Ghandehari H. Influence of Geometry, Porosity, and Surface Characteristics of Silica Nanoparticles on Acute Toxicity: Their Vasculature Effect and Tolerance Threshold. ACS Nano. 2012; 6:2289–301. [PubMed: 22364198]
12. Fatieiev Y, Croissant JG, Julfakyan K, Deng L, Anjum DH, Gurinov A, Khashab NM. Enzymatically Degradable Hybrid Organic-Inorganic Bridged Silsesquioxane Nanoparticles for in Vitro Imaging. Nanoscale. 2015; 7:15046–15050. [PubMed: 26165456]
13. Maggini L, Travaglini L, Cabrera I, Castro-Hartmann P, De Cola L. Biodegradable Peptide–Silica Nanodonuts. Chem - Eur J. 2016; 22:3697–3703. [PubMed: 26880470]

14. Croissant JG, Fatieiev Y, Julfakyan K, Lu J, Emwas A-H, Anjum DH, Omar H, Tamanoi F, Zink JI, Khashab NM. Biodegradable Oxamide-Phenylene-Based Mesoporous Organosilica Nanoparticles with Unprecedented Drug Payloads for Delivery in Cells. Chem - Eur J. 2016; 22:14806–14811. [PubMed: 27258139]
15. Croissant JG, Mauriello-Jimenez C, Maynadier M, Cattoën X, Man MWC, Raehm L, Mongin O, Blanchard-Desce M, Garcia M, Gary-Bobo M. Synthesis of Disulfide-Based Biodegradable Bridged Silsesquioxane Nanoparticles for Two-Photon Imaging and Therapy of Cancer Cells. Chem Commun. 2015; 51:12324–12327.
16. Croissant J, Cattoën X, Man MWC, Gallud A, Raehm L, Trens P, Maynadier M, Durand J-O. Biodegradable Ethylene-Bis(Propyl)Disulfide-Based Periodic Mesoporous Organosilica Nanorods and Nanospheres for Efficient in-Vitro Drug Delivery. Adv Mater. 2014; 26:6174–6180. [PubMed: 25042639]
17. Maggini L, Cabrera I, Ruiz-Carretero A, Prasetyanto EA, Robinet E, De Cola L. Breakable Mesoporous Silica Nanoparticles for Targeted Drug Delivery. Nanoscale. 2016; 8:7240–7247. [PubMed: 26974603]
18. Vivero-Escoto JL, Rieter WJ, Lau H, Huxford-Phillips RC, Lin W. Biodegradable Polysilsesquioxane Nanoparticles as Efficient Contrast Agents for Magnetic Resonance Imaging. Small. 2013; 9:3523–31. [PubMed: 23613450]
19. Omar H, Croissant JG, Alamoudi K, Alsaiari S, Alradwan I, Majrashi MA, Anjum DH, Martins P, Laamarti R, Eppinger J, et al. Biodegradable Magnetic Silica@Iron Oxide Nanovectors with Ultra-Large Mesopores for High Protein Loading, Magnetothermal Release, and Delivery. J Controlled Release. 2016; In Press. doi: 10.1016/j.jconrel.2016.11.032
20. Caracciolo G, Callipo L, De Sanctis SC, Cavaliere C, Pozzi D, Laganà A. Surface Adsorption of Protein Corona Controls the Cell Internalization Mechanism of Dc-Chol–Dope/DNA Lipoplexes in Serum. Biochim Biophys Acta, Biomembr. 2010; 1798:536–543.
21. Lee P, Knight R, Smit JM, Wilschut J, Griffin DE. A Single Mutation in the E2 Glycoprotein Important for Neurovirulence Influences Binding of Sindbis Virus to Neuroblastoma Cells. J Virol. 2002; 76:6302–6310. [PubMed: 12021363]
22. Pyrgiotakis G, Blattmann CO, Pratsinis S, Demokritou P. Nanoparticle-Nanoparticle Interactions in Biological Media by Atomic Force Microscopy. Langmuir. 2013; 29:11385–11395. [PubMed: 23978039]
23. Wei Y, Li X, Zhang R, Liu Y, Wang W, Ling Y, El-Toni AM, Zhao D. Periodic Mesoporous Organosilica Nanocubes with Ultrahigh Surface Areas for Efficient Co2 Adsorption. Sci Rep. 2016; 6:20769. [PubMed: 26868049]
24. Alsyouri HM, Abu-Daabes MA, Alassali A, Lin JY. Ordered Mesoporous Silica Prepared by Quiescent Interfacial Growth Method - Effects of Reaction Chemistry. Nanoscale Res Lett. 2013; 8:484. [PubMed: 24237719]
25. Yoganathan RB, Mammucari R, Foster NR. A Green Method for Processing Polymers Using Dense Gas Technology. Materials. 2010; 3:3188–3203.
26. Aznar E, Villalonga R, Gimenez C, Sancenon F, Marcos MD, Martinez-Manez R, Diez P, Pingarron JM, Amoros P. Glucose-Triggered Release Using Enzyme-Gated Mesoporous Silica Nanoparticles. Chem Commun. 2013; 49:6391–6393.
27. Saikia J, Yazdimamaghani M, Hadipour Moghaddam SP, Ghandehari H. Differential Protein Adsorption and Cellular Uptake of Silica Nanoparticles Based on Size and Porosity. ACS Appl Mater Interfaces. 2016; 8:34820–34832. [PubMed: 27998138]
28. Hoffmann F, Cornelius M, Morell J, Froba M. Silica-Based Mesoporous Organic-Inorganic Hybrid Materials. Angew Chem, Int Ed. 2006; 45:3216–51.
29. Van Der Voort P, Esquivel D, De Canck E, Goethals F, Van Driessche I, Romero-Salguero FJ. Periodic Mesoporous Organosilicas: From Simple to Complex Bridges; a Comprehensive Overview of Functions, Morphologies and Applications. Chem Soc Rev. 2013; 42:3913–3955. [PubMed: 23081688]
30. Cheng R, Feng F, Meng F, Deng C, Feijen J, Zhong Z. Glutathione-Responsive Nano-Vehicles as a Promising Platform for Targeted Intracellular Drug and Gene Delivery. J Controlled Release. 2011; 152:2–12.

31. Montero D, Tachibana C, Rahr Winther J, Appenzeller-Herzog C. Intracellular Glutathione Pools Are Heterogeneously Concentrated. Redox Biol. 2013; 1:508–513. [PubMed: 24251119]
32. Lushchak VI. Glutathione Homeostasis and Functions: Potential Targets for Medical Interventions. J Amino Acids. 2012; 2012doi: 10.1155/2012/736837
33. Wu G, Fang Y-Z, Yang S, Lupton JR, Turner ND. Glutathione Metabolism and Its Implications for Health. J Nutr. 2004; 134:489–492. [PubMed: 14988435]
34. Arner ES, Holmgren A. Physiological Functions of Thioredoxin and Thioredoxin Reductase. Eur J Biochem. 2000; 267:6102–9. [PubMed: 11012661]
35. Senft AP, Dalton TP, Shertzer HG. Determining Glutathione and Glutathione Disulfide Using the Fluorescence Probe O-Phthalaldehyde. Anal Biochem. 2000; 280:80–6. [PubMed: 10805524]
36. Herd HL, Malugin A, Ghandehari H. Silica Nanoconstruct Cellular Toleration Threshold in Vitro. J Controlled Release. 2011; 153:40–8.
37. Gustafson HH, Holt-Casper D, Grainger DW, Ghandehari H. Nanoparticle Uptake: The Phagocyte Problem. Nano Today. 2015; 10:487–510. [PubMed: 26640510]
38. Slowing II, Wu CW, Vivero-Escoto JL, Lin VS. Mesoporous Silica Nanoparticles for Reducing Hemolytic Activity Towards Mammalian Red Blood Cells. Small. 2009; 5:57–62. [PubMed: 19051185]
39. Sun L, Li Y, Liu X, Jin M, Zhang L, Du Z, Guo C, Huang P, Sun Z. Cytotoxicity and Mitochondrial Damage Caused by Silica Nanoparticles. Toxicol In Vitro. 2011; 25:1619–29. [PubMed: 21723938]
40. Park Y-H, Bae HC, Jang Y, Jeong SH, Lee HN, Ryu W-I, Yoo MG, Kim Y-R, Kim M-K, Lee JK, Jeong J, Son SW. Effect of the Size and Surface Charge of Silica Nanoparticles on Cutaneous Toxicity. Mol Cell Toxicol. 2013; 9:67–74.
41. Maeda H, Wu J, Sawa T, Matsumura Y, Hori K. Tumor Vascular Permeability and the EPR Effect in Macromolecular Therapeutics: A Review. J Controlled Release. 2000; 65:271–84.
42. Hu L, Mao Z, Zhang Y, Gao C. Influences of Size of Silica Particles on the Cellular Endocytosis, Exocytosis and Cell Activity of HepG2 Cells. J Nanosci Lett. 2011; 1:1–16.
43. Phan UT, Arunachalam B, Cresswell P. Gamma-Interferon-Inducible Lysosomal Thiol Reductase (Gilt). Maturation, Activity, and Mechanism of Action. J Biol Chem. 2000; 275:25907–25914. [PubMed: 10852914]
44. Collins DS, Unanue ER, Harding CV. Reduction of Disulfide Bonds within Lysosomes Is a Key Step in Antigen Processing. J Immunol. 1991; 147:4054–4059. [PubMed: 1721638]
45. Berg T, Gjøen T, Bakke O. Physiological Functions of Endosomal Proteolysis. Biochem J. 1995; 307:313–326. [PubMed: 7733863]
46. Arunachalam B, Phan UT, Geuze HJ, Cresswell P. Enzymatic Reduction of Disulfide Bonds in Lysosomes: Characterization of a Gamma-Interferon-Inducible Lysosomal Thiol Reductase (Gilt). Proc Natl Acad Sci U S A. 2000; 97:745–750. [PubMed: 10639150]
47. Ai, H-x, Zhang, Z-z, Shen, Y-f, Zhang, J-x, Zhou, X-m, Min, C., Zhu, S-y, Zhang, S-q. Molecular Structure, Phylogenetic Analysis, Tissue Distribution, and Function Characterization of Interferon-Γ-Inducible Lysosomal Thiol Reductase (Gilt) Gene in Sheep (Ovis Aries). Vet Immunol Immunopathol. 2011; 140:329–334. [PubMed: 21334075]
48. Hastings KT, Cresswell P. Disulfide Reduction in the Endocytic Pathway: Immunological Functions of Gamma-Interferon-Inducible Lysosomal Thiol Reductase. Antioxid Redox Signaling. 2011; 15:657–68.

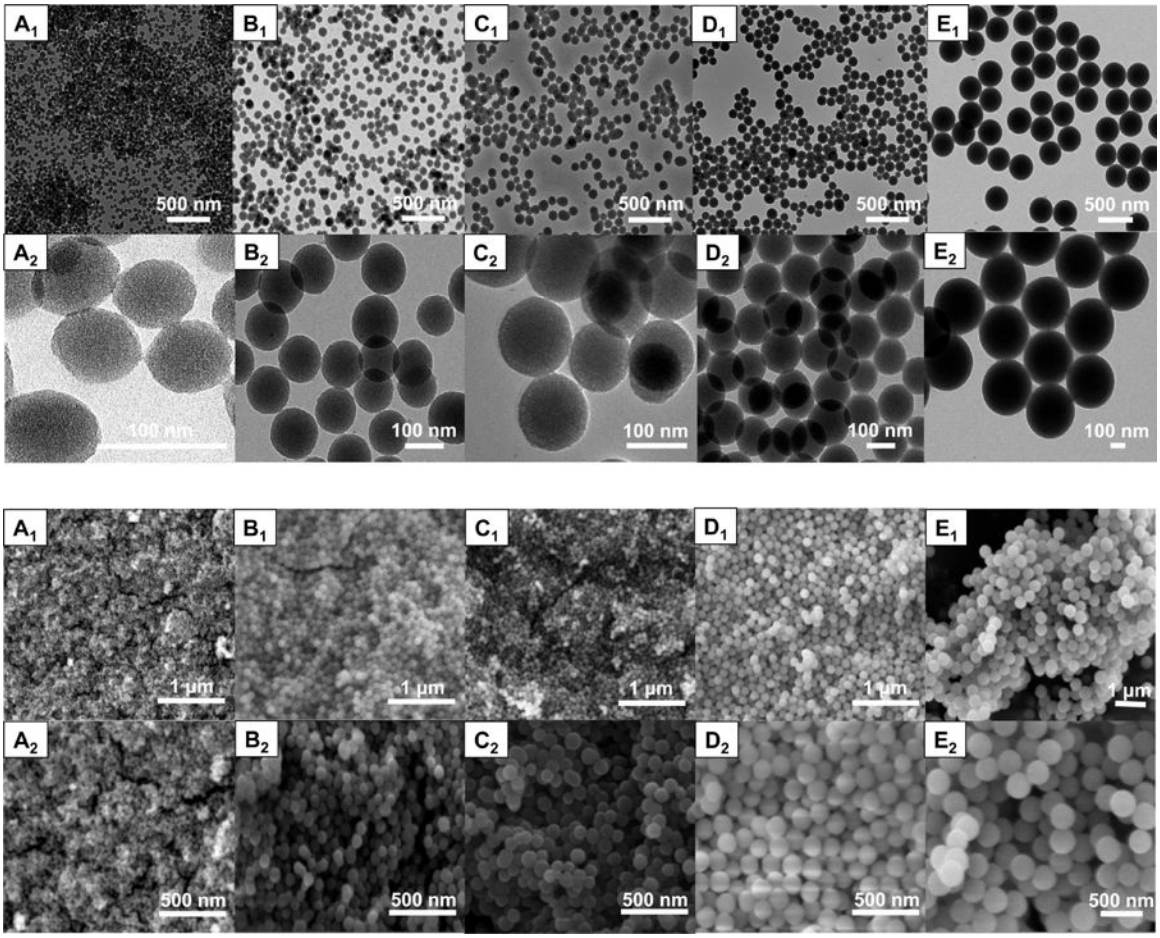

Figure 1.

TEM (top) and SEM (bottom) images of the nanoparticles at two magnifications. Nanoparticles from left to right: (A_1, A_2) 60 Mesoporous D; (B_1, B_2) 110 Mesoporous D; (C_1, C_2) 110 Mesoporous T; (D_1, D_2) 120 Nonporous D; and (E_1, E_2) 330 Nonporous D. Both TEM and SEM images indicate that highly uniform nanoparticles with low polydispersity were synthesized. On the basis of the images, nonporous nanoparticles had denser structure, with a smoother surface in larger nanoparticles.

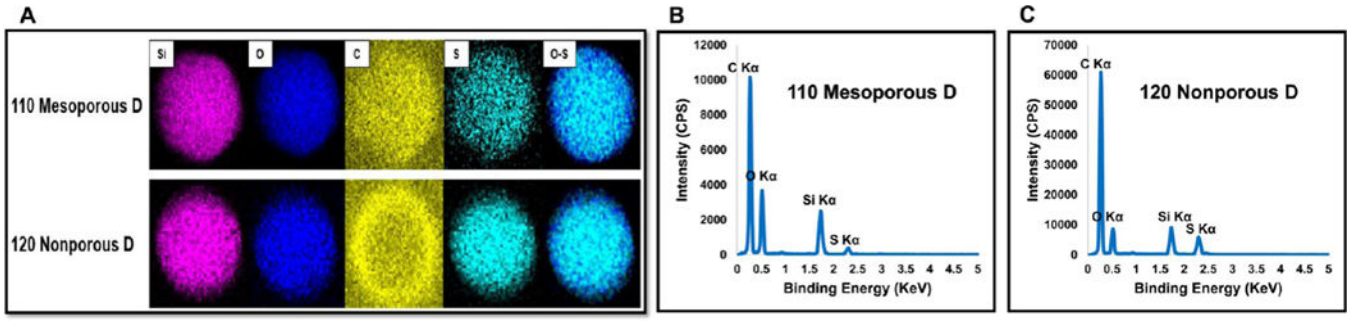

Figure 2.

(A) STEM images; (B) and (C) STEM spectra for 110 Mesoporous D and 120 Nonporous D nanoparticles. The images show homogeneous distribution of sulfur in both nanoparticles. Spectra confirm that nonporous nanoparticles have higher sulfur density than mesoporous nanoparticles.

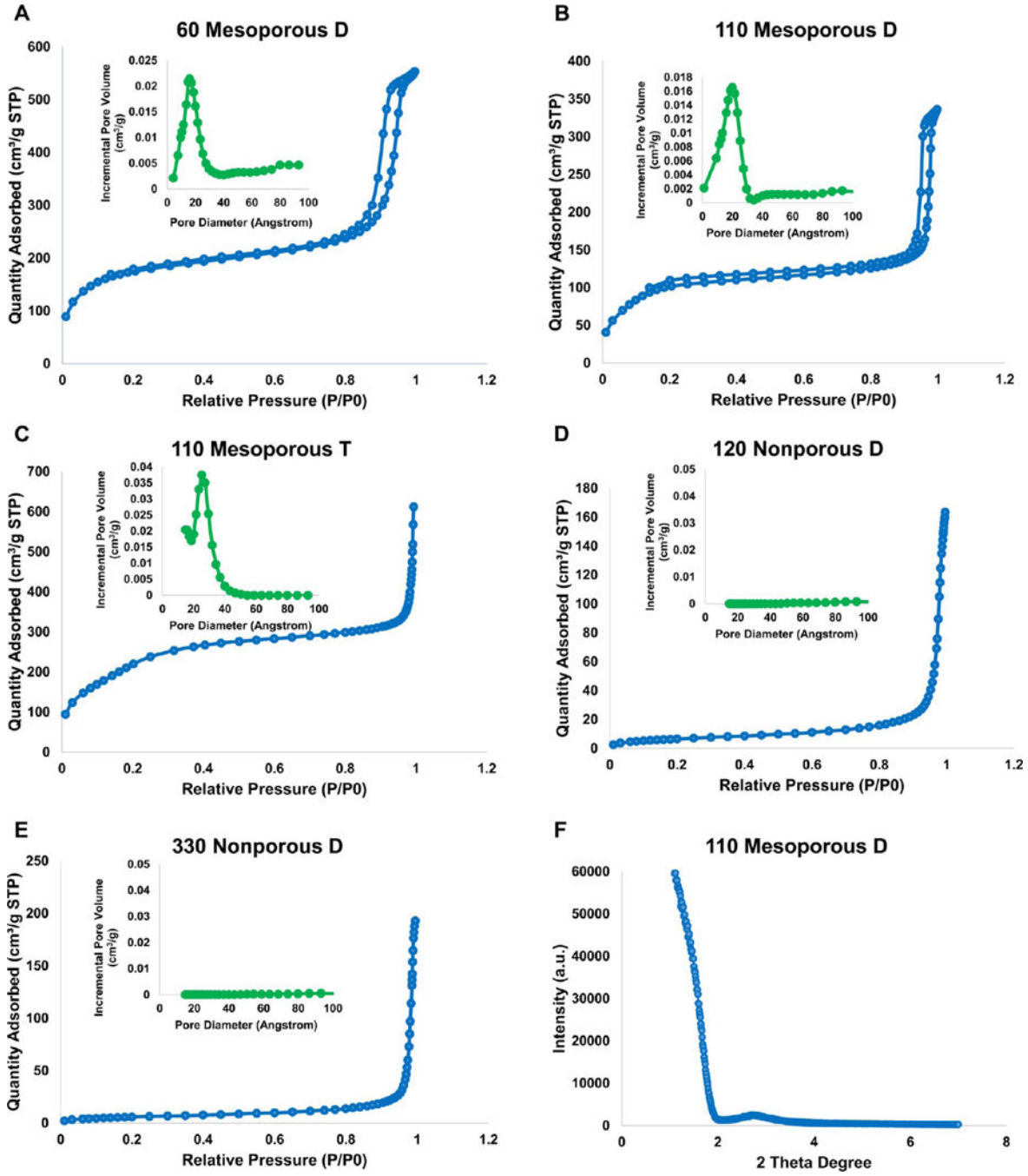

Figure 3.

Nitrogen adsorption–desorption isotherms: (A) 60 Mesoporous D; (B) 110 Mesoporous D; (C) 110 Mesoporous T; (D) 120 Nonporous D; and (E) 330 Nonporous D. On the basis of IUPAC classification, isotherms in A–C indicate mesoporous structure, while those in D and E are associated with nonporous structure. Green insets are pore diameter distribution plots for each nanoparticle in angstrom. (F) XRD graph of 110 Mesoporous D nanoparticles does not show the typical Bragg peaks and confirms the disordered pore structure of these nanoparticles.

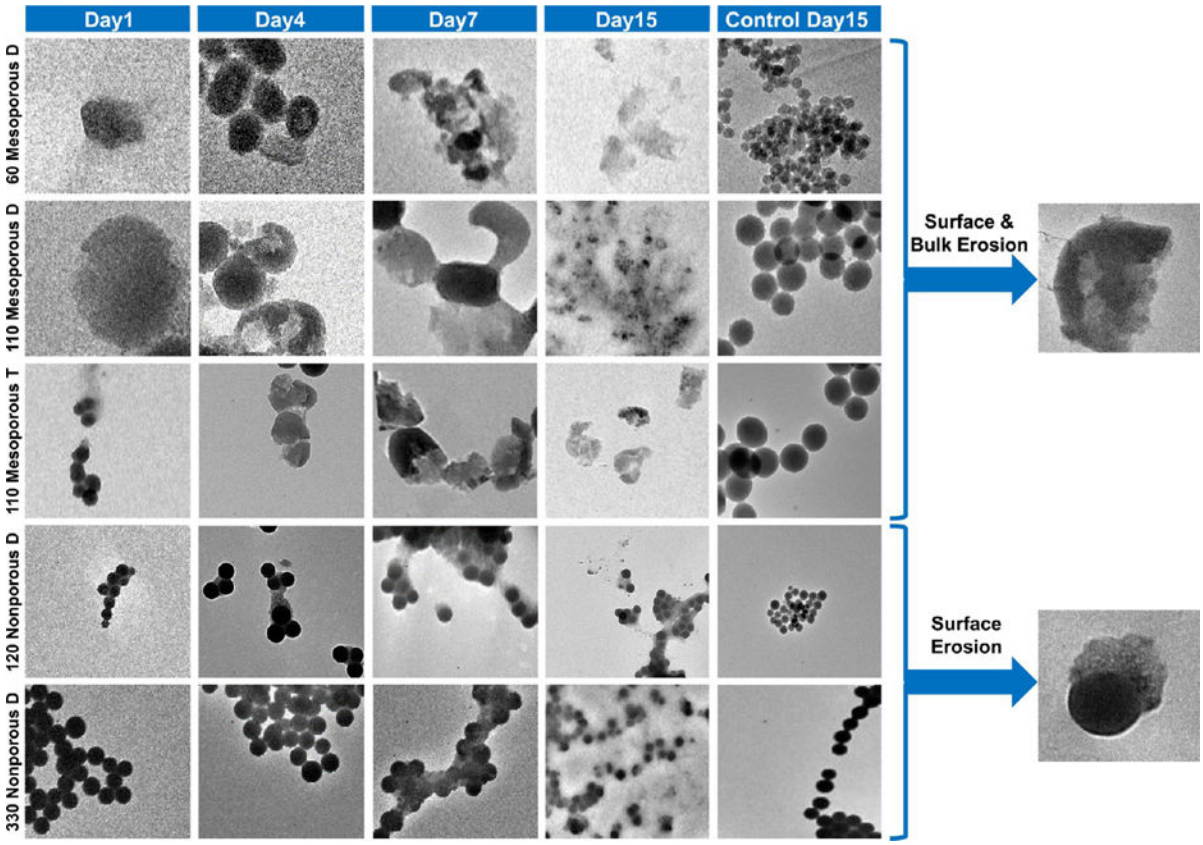

Figure 4.

In vitro degradation of the nanoparticles under 8 mM GSH at 37 °C and pH 7.2. For mesoporous nanoparticles, surface and bulk erosion started fromat day 1, followed by higher degradation after day 15 due to high surface area. Nonporous nanoparticles showed surface erosion within 15 days. As evident in control images, degradation of these nanoparticles was not observable in the absence of GSH after 15 days.

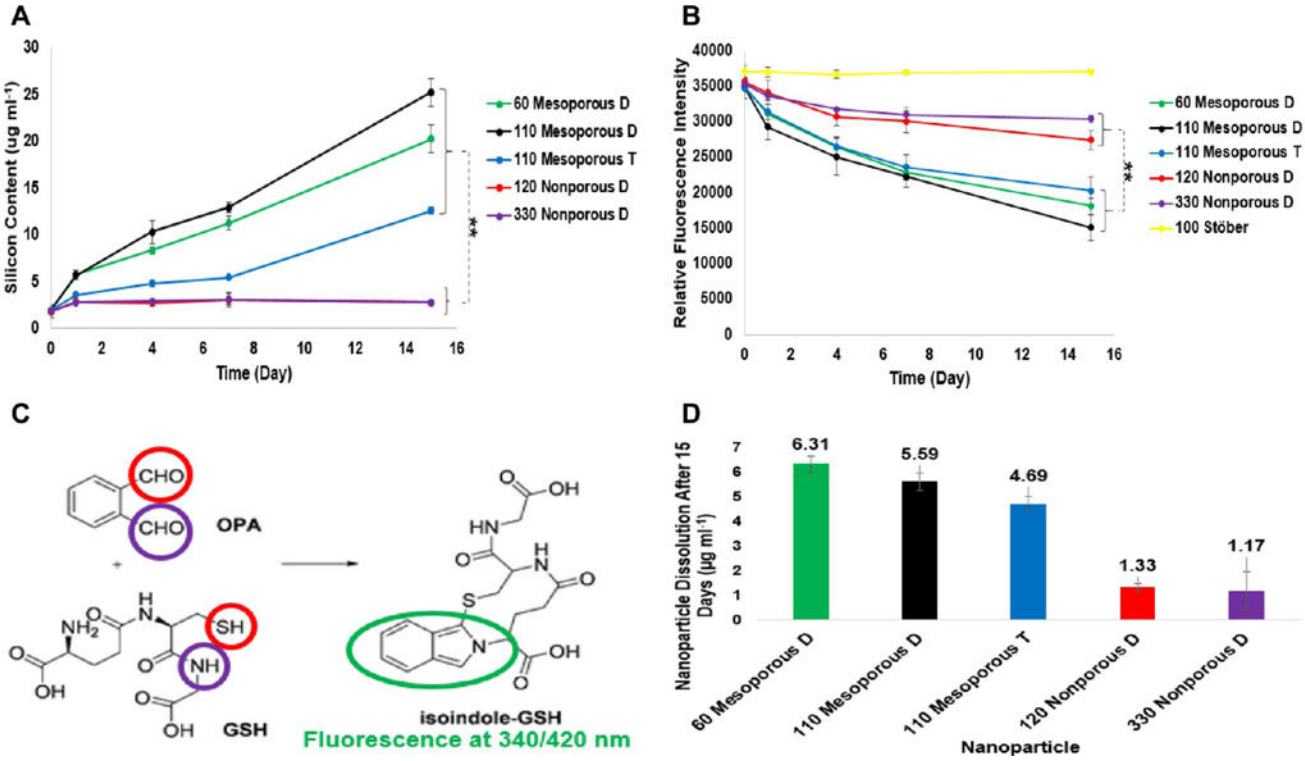

Figure 5.

Degradation kinetics of the nanoparticles: (A) On the basis of ICP-MS, mesoporous nanoparticles degraded faster than nonporous nanoparticles, and (B) OPA-GSH assay confirms more consumption of GSH in mesoporous nanoparticles than in nonporous nanoparticles. (C) Schematic of the reaction between GSH and OPA. OPA with two aldehyde groups can bind selectively to sulfur and nitrogen atoms in GSH leading to the formation of isoindole ring in GSH. The latter compound has fluorescence at excitation/emission wavelengths of 340/420 nm. (D) Nanoparticle dissolution after 15 days in DI water without GSH. Data are mean ± SD ($n = 3$). **, data are statistically different.

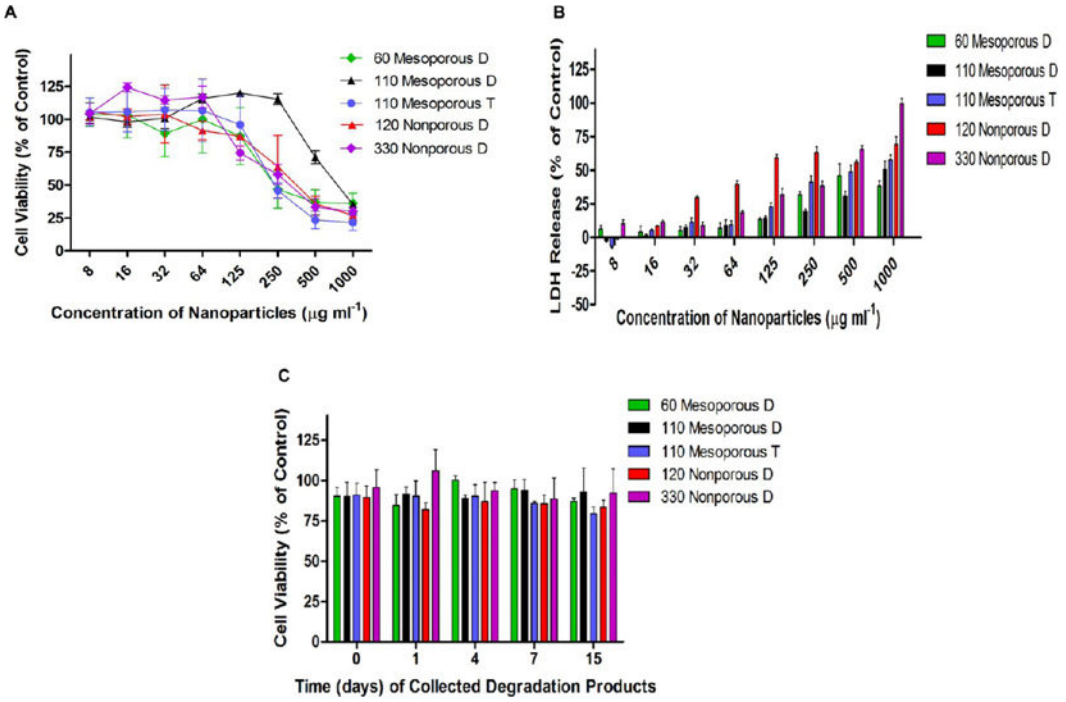

Figure 6.

(A) Cytotoxicity and (B) membrane integrity evaluation of the degradable nanoparticles after 24 h of incubation in RAW 264.7 macrophages via CCK-8 and LDH assays, respectively. Both assays confirm the concentration-dependent toxicity of these nanoparticles. (C) Cytotoxicity evaluation of the degradation products collected at different time points using CCK-8 assay. Results indicate more than 85% cell viability over the 15 day period of study. Data are mean ± SD (n = 3).

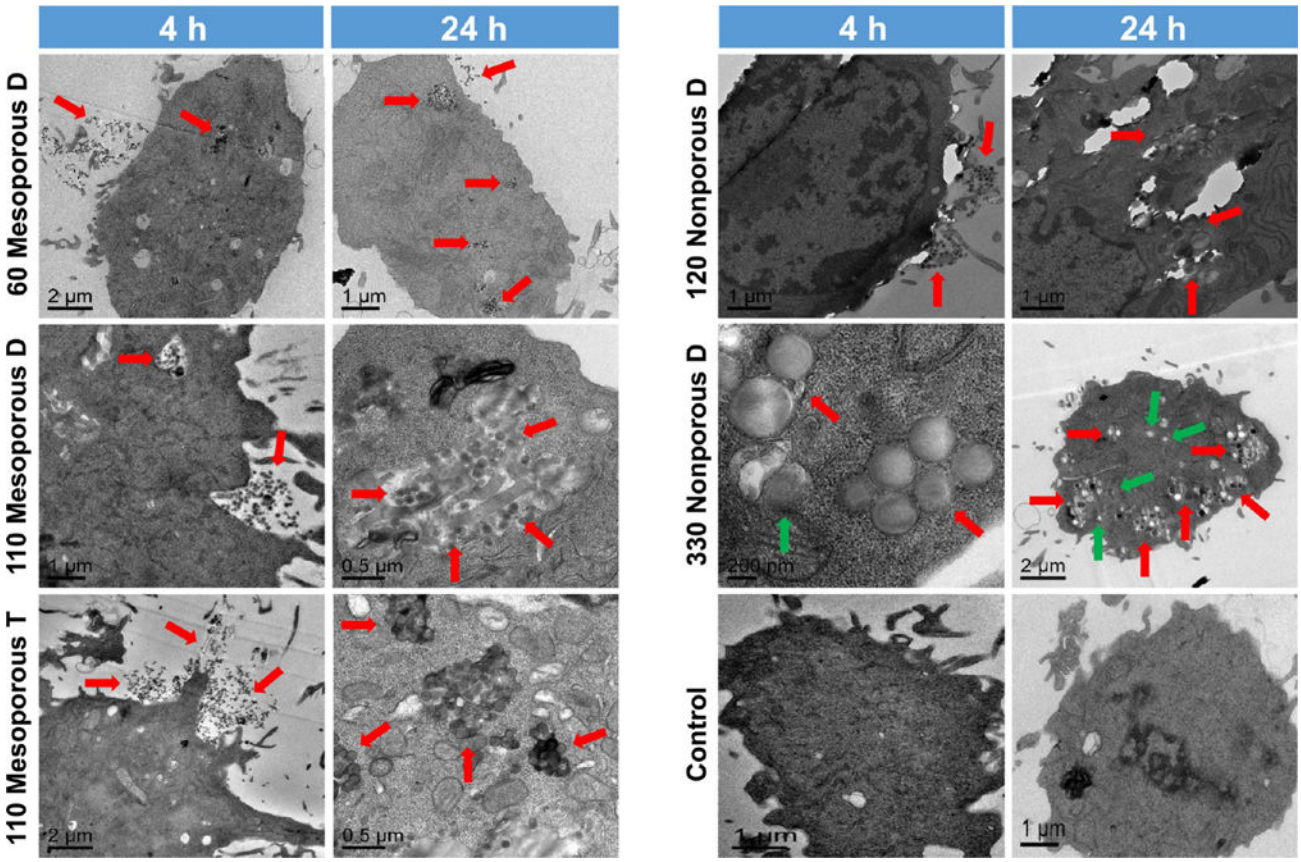

Figure 7.

Cell uptake observed by TEM after 4 and 24 h of incubation of 80 μg mL^{-1} nanoparticles in RAW 264.7 macrophages. Nanoparticles were taken up in a time-dependent pattern and trapped in endosomal vacuoles. A few larger nanoparticles (especially 330 nm shown as green arrows) were isolated as individual nanoparticles.

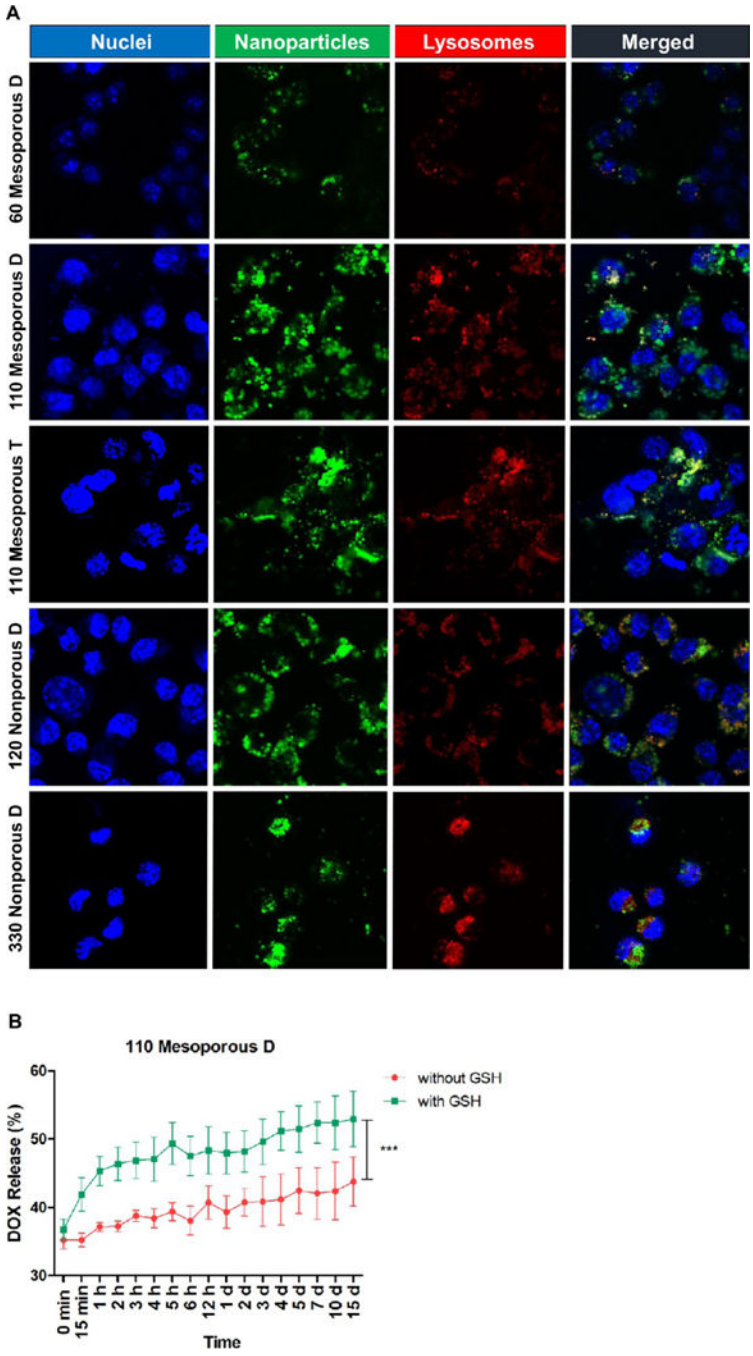

Figure 8.

(A) CLSM images showing co-localization of 80 μg mL^{-1} nanoparticles after 24 h of incubation in RAW 264.7 macrophages. Nuclei were stained in blue with Hoechst 33342 dye. Nanoparticles appear with the green fluorescence of FITC. Lysosomes were stained in red via LysoTracker Deep Red dye. As shown, nanoparticles accumulated in the endolysosomal compartments and in the perinuclear regions. (B) DOX release from 110 Mesoporous D nanoparticles. The amount of release in the presence of GSH was

significantly higher than that in the absence of GSH. Data are mean ± SD (n = 3). ***, statistically significant difference between the two study groups (P_{value} < 0.001).

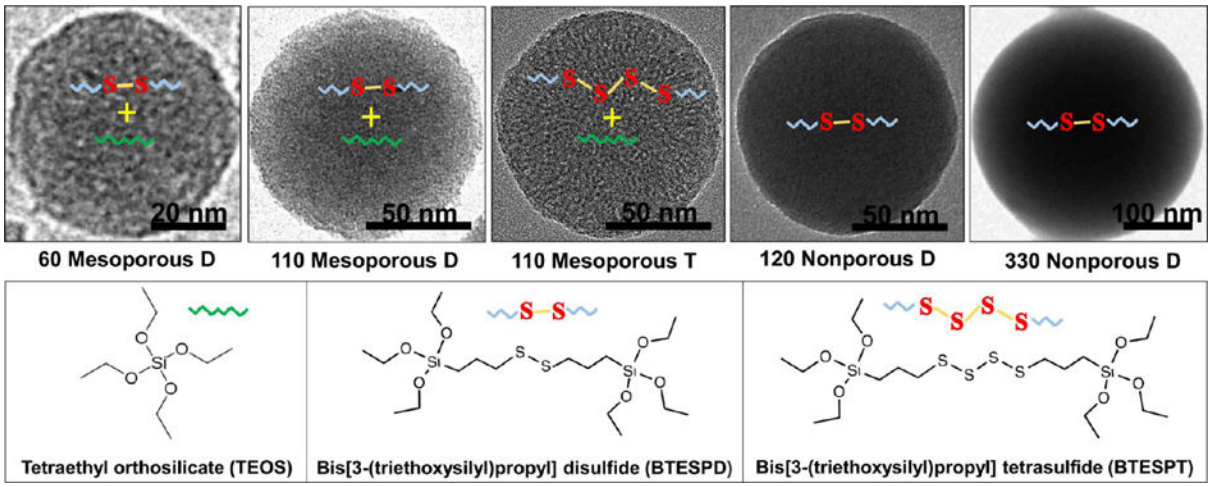

Scheme 1. TEM Images of Nanoparticles and Structures of Precursors[a]

[a]Top panel: representative transmission electron microscopy (TEM) images of the degradable nanoparticles. Bottom panel: precursors used to fabricate the nanoparticles. Mesoporous nanoparticles were synthesized using the combination of two precursors (TEOS and BTESPD for the fabrication of disulfide-based nanoparticles; TEOS and BTESPT for the fabrication of tetrasulfide-based nanoparticle), while nonporous nanoparticles were made by only disulfide-based precursor (BTESPD).

Table 1

Size and Zeta Potential of the Nanoparticles in DI Water, Media + 10% FBS, and PBS[a]

	hydrodynamic diameter (nm) measured by DLS			zeta potential (mV) at 25 °C		
nanoparticle	**deionized (DI) water**	**media + 10% FBS**	**diameter (nm) measured by TEM**	**DI water pH 7.2**	**media + 10% FBS**	**PBS pH 7.2**
60 Mesoporous D	79 ± 2	216 ± 15	58 ± 7	−32 ± 2	−10 ± 1	−8 ± 2
110 Mesoporous D	165 ± 2	178 ± 57	108 ± 11	−32 ± 1	−8 ± 1	−7
110 Mesoporous T	162 ± 8	218 ± 52	110 ± 9	−27 ± 1	−11	−4
120 Nonporous D	148 ± 4	219 ± 28	124 ± 9	−33 ± 2	−7.5	−8
330 Nonporous D	367 ± 2	433 ± 12	332 ± 6	−29 ± 2	−9 ± 1	−11 ± 1

[a]Data are mean ± SD ($n = 3$).

Table 2

Nitrogen Adsorption–Desorption Features of the Synthesized SiO_2 NPs[a]

nanoparticle	surface area (m^2 g^{-1})	total pore area (m^2 g^{-1})	average pore diameter (nm)
60 Mesoporous D	614	215	1.7
110 Mesoporous D	366	140	2
110 Mesoporous T	808	313	2.7
120 Nonporous D	24	N/A	N/A
330 Nonporous D	21	N/A	N/A

[a]N/A: not applicable

Table 3

IC_{50} Values for the Nanoparticles Measured from CCK-8 Assay in RAW 264.7 Macrophages

nanoparticle	IC_{50} (μg mL^{-1})[a]
60 Mesoporous D	365 ± 37
110 Mesoporous D	705 ± 17
110 Mesoporous T	233 ± 42
120 Nonporous D	343 ± 41
330 Nonporous D	220 ± 93

[a]Data are mean ± SD (n = 3).